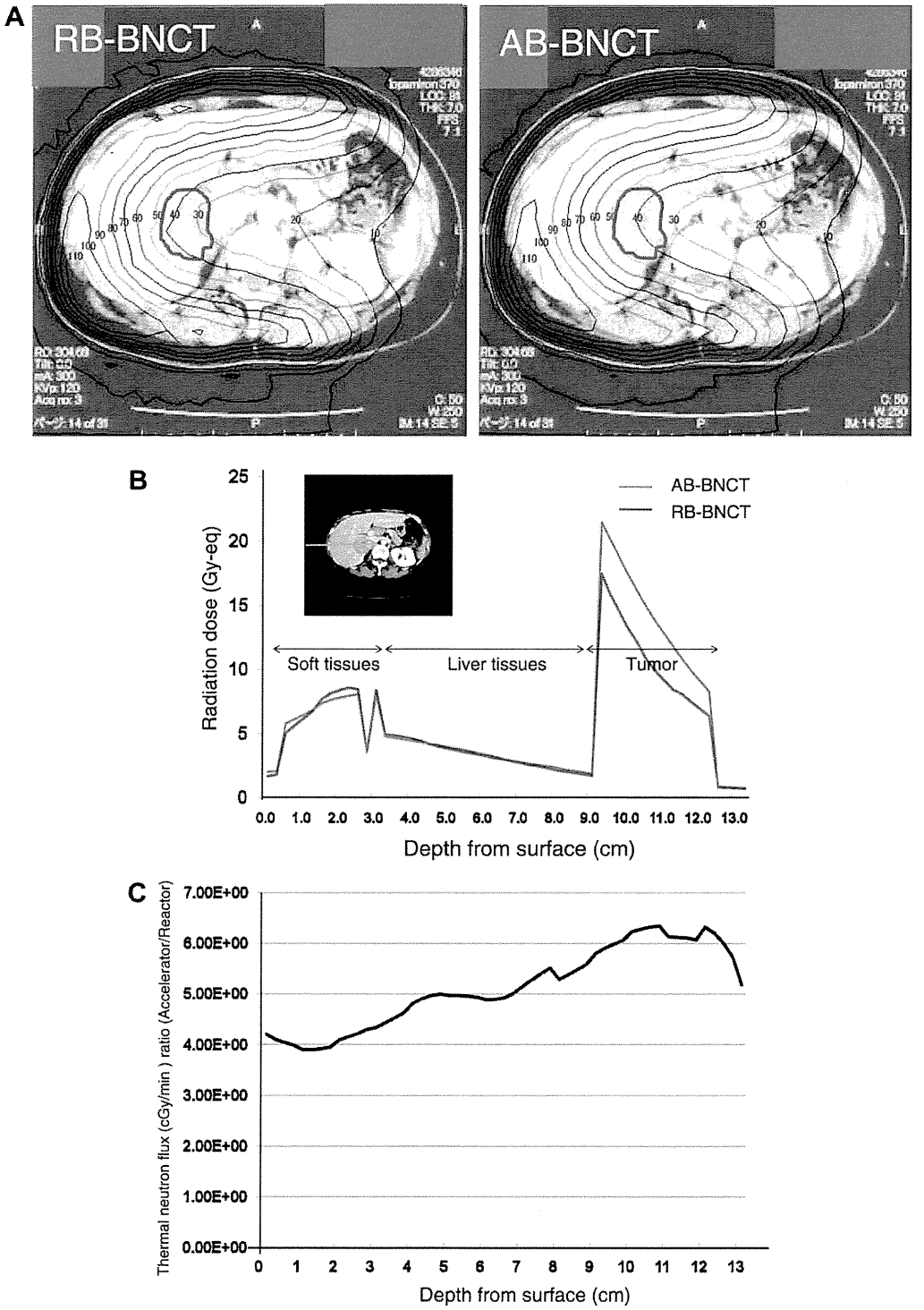

Fig. 3. (A) Comparison of isodose distribution between RB-BNCT and AB-BNCT. The liver tumor is contoured with a solid red line. (B) Depth–dose distribution profiles along the right neutron beam axis, which passed into the deep-seated liver tumor located at a depth of 9.5–12.5 cm. A yellow arrow on the CT image indicates the beam axis. (C) Depth–thermal neutron flux ratio (AB-BCNT to RB-BNCT) profiles along the same beam axis as that in (B).

BNCT, under conditions in which the mean doses delivered to normal liver or lung are equal. This advantage of AB-BNCT over RB-BNCT was especially evident in BNCT for deep-seated multiple liver tumors. As shown in Table 2, AB-BNCT delivered significantly greater doses to liver tumors than RB-BNCT did. As shown in Fig. 2, the AB-BNCT system provided a higher peak energy (near 10 keV) in its neutron spectrum compared with RB-BNCT. The higher energy peak of the AB-BNCT system is well suited for generating a thermal neutron flux distribution suitable for deep-seated tumors and provides a larger thermal neutron fluence to areas deep within the body compared to the RB-BNCT system. However, while the epi-thermal neutron beam of HWNIF in the KUR has a softer spectrum and the near-10-keV component is not significant, the higher epi-thermal neutron component

Table 3
Irradiation time and DVH parameters showing averages (with range) for MPM tumors and normal lung.

Neutron source	Irradiation time (min)	Tumor			Ipsilateral lung			Contralateral lung			Liver*		
		D_{max} (Gy-eq)	D_{mean} (Gy-eq)	D_{min} (Gy-eq)	D_{max} (Gy-eq)	D_{mean} (Gy-eq)	D_{min} (Gy-eq)	D_{max} (Gy-eq)	D_{mean} (Gy-eq)	D_{min} (Gy-eq)	D_{max} (Gy-eq)	D_{mean} (Gy-eq)	D_{min} (Gy-eq)
KUR	134.7 (117.4–156.4)	40.0 (35.0–42.3)	19.9 (19.3–20.7)	4.3 (3.0–6.1)	7.7 (7.1–8.1)	5.0†	2.2 (1.8–2.5)	5.3 (4.7–6.8)	1.4 (1.2–1.9)	0.4 (0.3–0.6)	10.4 (10.0–10.8)	5.0 (4.6–5.2)	0.9 (0.8–1.0)
Accelerator	29.9 (26.3–33.3)	36.4 (33.0–38.3)	20.2 (19.7–21.0)	4.6 (3.4–6.4)	7.3 (6.9–7.5)	5.0†	2.3 (1.8–2.6)	4.9 (4.2–6.0)	1.3 (1.1–1.8)	0.3 (0.2–0.5)	9.7 (9.2–10.2)	5.0 (4.7–5.2)	0.8 (0.7–0.8)

Abbreviations: DVH = dose-volume histogram; MPM = malignant pleural mesothelioma; KUR = Kyoto University Research Reactor.
* The average (range) of DVH data for liver was estimated using the data for three cases with right MPM.
† The mean dose to the liver normalized to 5.0 Gy-Eq.

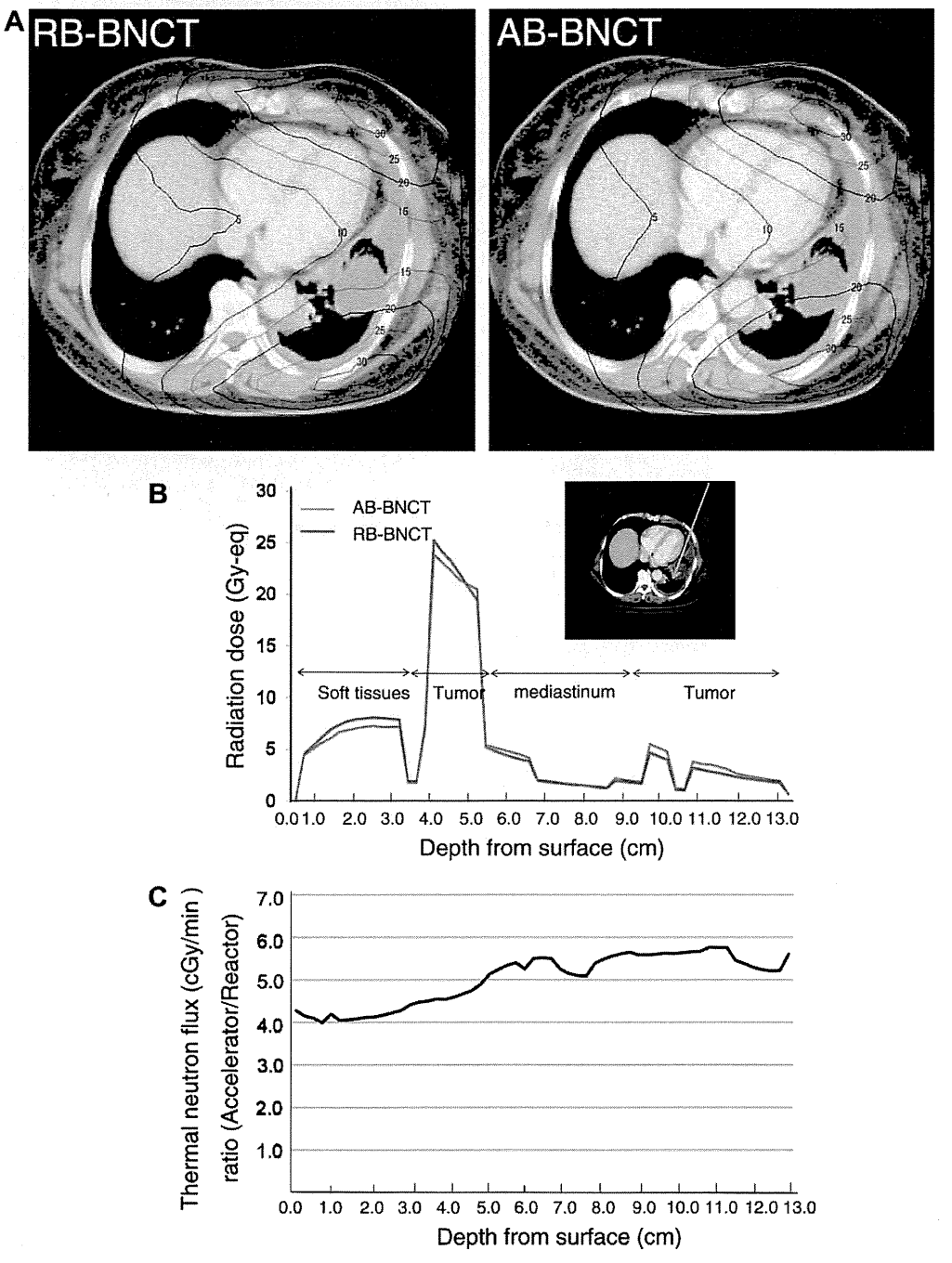

Fig. 4. (A) Comparison of isodose distribution between RB-BNCT and AB-BNCT. (B) Depth–dose distribution profile along the anterior-oblique neutron beam axis in the case of BNCT for MPM. A yellow arrow on the CT image indicates the beam axis. (C) Depth–thermal neutron flux ratio (AB-BCNT to RB-BNCT) profiles along the same beam axis as that in (B).

included in the KUR beam is effective for enlarging the thermal neutron flux at parts deep within the body. This is because the RB-BNCT system can maximize the dose sent to deep-seated tumors near 10 cm, as well as the AB-BNCT system (Figs. 3B and 4B).

Some authors have already reported the advantage of AB-BNCT for deep-seated brain tumors over RB- BNCT using a head phantom. Burlon et al. have reported that AB-BNCT can treat brain tumors that are ~2.0 cm deeper than those treated with RB-BNCT [19]. Blue et al. have reported that, for treatment of brain tumors, compared with RB-BNCT, AB-BNCT can create a neutron field with a significantly better field quality (by a factor of 1.2), which is judged by the dose that can be delivered to a tumor at a depth of 6 cm [20]. The present study is believed to be the first to describe the advantages of AB-BNCT over RB-BNCT in the treatment of body trunk tumors, multiple liver tumors and MPM, apart from brain tumors.

We are preparing to undertake clinical trials with our AB-BNCT system to get an approval as a medical device from the Pharmaceuticals and Medical Devices Agency (PMDA), a Japanese regulatory agency. This approval is a prerequisite before the AB-BNCT system can be constructed at medical institutes. As revealed in the present study, AB-BNCT has the potential to be applied to multiple liver tumors and MPM. The patients with multiple liver tumors, including metastatic tumors or hepatocellular carcinomas, are much greater in number than malignant gliomas or melanomas, which have been treated with BNCT in Japan, the United States and Europe. Selective high-LET irradiation to tumor cells by BNCT has the potential to shed new light on the best way to treat multiple metastatic tumors in lung or brain and pleuritis carcinomatosis. Extending the application of BNCT to many malignancies will lead to further progress in the field of BNCT. After approval of the AB-BNCT system as a medical device, it will be on the market and installed in existing hospitals.

In conclusion, the AB-BNCT system constructed at our institute has the ability to deliver three- or four-port irradiation in the treatment of multiple liver tumors and MPM within a reasonable treatment time (30–60 min). In addition, the AB-BNCT system has advantages over RB-BNCT for the treatment of deep-seated tumors. AB-BNCT has the potential to be a promising treatment option for patients with multiple liver tumors and MPM.

References

[1] Coderre JA, Morris GM. The radiation biology of boron neutron capture therapy. Radiat Res 1999;151:1–18.
[2] Barth RF, Joensuu H. Boron neutron capture therapy for the treatment of glioblastomas and extracranial tumours: as effective, more effective or less effective than photon irradiation? Radiother Oncol 2007;82:119–22.
[3] Suzuki M, Masunaga S, Kinashi Y, et al. Intra-arterial administration of sodium borocaptate (BSH)/lipiodol emulsion delivers B-10 to liver tumors highly selectively for boron neutron capture therapy: experimental studies in the rat liver model. Int J Radiat Oncol Biol Phys 2004;59:260–6.
[4] Suzuki M, Sakurai Y, Masunaga S, et al. Preliminary experimental study of boron neutron capture therapy for malignant tumors spreading in thoracic cavity. Jpn J Clin Oncol 2007;37:245–9.
[5] Suzuki M, Sakurai Y, Masunaga S, Kinashi Y, Nagata K, Ono K. Dosimetric study of boron neutron capture therapy with borocaptate sodium (BSH)/lipiodol emulsion (BSH/lipiodol-BNCT) for treatment of multiple liver tumors. Int J Radiat Oncol Biol Phys 2004;58:892–6.
[6] Suzuki M, Sakurai Y, Masunaga S, et al. Feasibility of boron neutron capture therapy (BNCT) for malignant pleural mesothelioma from a viewpoint of dose distribution analysis. Int J Radiat Oncol Biol Phys 2006;66:1584–9.
[7] Suzuki M, Sakurai Y, Hagiwara S, et al. First attempt of boron neutron capture therapy (BNCT) for hepatocellular carcinoma. Jpn J Clin Oncol 2007;37:376–81.
[8] Suzuki M, Endo K, Satoh H, et al. A novel concept of treatment of diffuse or multiple pleural tumors by boron neutron capture therapy (BNCT). Radiother Oncol 2008;88:192–5.
[9] Lee CL, Zhou XL, Kudchadker RJ, Harmon F, Harker YD. A Monte Carlo dosimetry-based evaluation of the $^{7}Li(p,n)^{7}Be$ reaction near threshold for accelerator boron neutron capture therapy. Med Phys 2000;27:192–202.
[10] Tanaka H, Sakurai Y, Suzuki M, et al. An epithermal neutron generator based on the Be(p,n) reaction using a 30 MeV proton cyclotron accelerator at KURRI. In: Zonta A, Altieri S, Roveda L, Barth R, editors. 13th International Congress on Neutron Capture Therapy "A new option against cancer". Roma: ENEA; 2008. p. 510–3.
[11] IAEA. Current status of neutron capture therapy. In: IAEA TECDOC 1223, Vienna: IAEA; 2001. p. 6–8.
[12] Sakurai Y, Kobayashi T. Controllability of depth dose distribution for neutron capture therapy at the heavy water neutron irradiation facility of Kyoto University Research Reactor. Med Phys 2002;29:2338–50.
[13] Sakurai Y, Kobayashi T. The medical-irradiation characteristics for neutron capture therapy at the heavy water neutron irradiation facility of Kyoto University Research Reactor. Med Phys 2002;29:2328–37.
[14] Kawabata S, Miyatake S, Kajimoto Y, et al. The early successful treatment of glioblastoma patients with modified boron neutron capture therapy. Report of two cases. J Neurooncol 2003;65:159–65.
[15] Kato I, Ono K, Sakurai Y, et al. Effectiveness of BNCT for recurrent head and neck malignancies. Appl Radiat Isot 2004;61:1069–73.
[16] Suzuki M, Masunaga S, Kinashi Y, et al. The effects of boron neutron capture therapy on liver tumors and normal hepatocytes in mice. Jpn J Cancer Res 2000;91:1058–64.
[17] Kiger JL, Kiger WS, Patel H, et al. Functional and histological assessment of the radiobiology of normal rat lung in BNCT. In: Nakagawa Y, Kobayashi T, Fukuda H, editors. Advances in neutron capture therapy 2006. Takamatsu: ISNCT; 2006. p. 85–8.
[18] Ono K, Nagata Y, Akuta K, Abe M, Ando K, Koike S. Frequency of micronuclei in hepatocytes following X and fast-neutron irradiations-an analysis by a linear-quadratic model. Radiat Res 1990;123:345–7.
[19] Burlon AA, Kreiner AJ. A comparison between a TESQ accelerator and a reactor as a neutron sources for BNCT. Nucl Instr Meth Phys Res B 2008;266:763–71.
[20] Blue TE, Yanch JC. Accelerator-based epithermal neutron sources for boron neutron capture therapy of brain tumors. J Neurooncol 2003;62:19–31.

Applied Radiation and Isotopes 67 (2009) S258–S261

Contents lists available at ScienceDirect

Applied Radiation and Isotopes

journal homepage: www.elsevier.com/locate/apradiso

Improvement of dose distribution in phantom by using epithermal neutron source based on the Be(p,n) reaction using a 30 MeV proton cyclotron accelerator

H. Tanaka [a,*], Y. Sakurai [a], M. Suzuki [a], T. Takata [a], S. Masunaga [a], Y. Kinashi [a], G. Kashino [a], Y. Liu [a], T. Mitsumoto [b], S. Yajima [b], H. Tsutsui [b], M. Takada [c], A. Maruhashi [a], K. Ono [a]

[a] Research Reactor Institute, Kyoto University, Asashiro-nishi 2-1010, Kumatori-cho, Osaka 590-0494, Japan
[b] Sumitomo Heavy Industries, Osaki 2-1-1, Shinagawa, Tokyo 141-6025, Japan
[c] National Institute of Radiological Sciences, Anagawa 4-9-1, Inage-ku, Chiba-shi 263-8555, Japan

ARTICLE INFO

Keywords:
Cyclotron-based neutron source
Proton cyclotron
Be(p,n) reaction

ABSTRACT

In order to generate epithermal neutrons for boron neutron capture therapy (BNCT), we proposed the method of filtering and moderating fast neutrons, which are emitted from the reaction between a beryllium target and 30 MeV protons accelerated by a cyclotron, using an optimum moderator system composed of iron, lead, aluminum, calcium fluoride, and enriched ^{6}LiF ceramic filter. At present, the epithermal-neutron source is under construction since June 2008 at Kyoto University Research Reactor Institute. This system consists of a cyclotron to supply a proton beam of about 1 mA at 30 MeV, a beam transport system, a beam scanner system for heat reduction on the beryllium target, a target cooling system, a beam shaping assembly, and an irradiation bed for patients.

In this article, an overview of the cyclotron-based neutron source (CBNS) and the properties of the treatment neutron beam optimized by using the MCNPX Monte Carlo code are presented. The distribution of the RBE (relative biological effectiveness) dose in a phantom shows that, assuming a ^{10}B concentration of 13 ppm for normal tissue, this beam could be employed to treat a patient with an irradiation time less than 30 min and a dose less than 12.5 Gy-eq to normal tissue. The CBNS might be an alternative to the reactor-based neutron sources for BNCT treatments.

1. Introduction

At first, the BNCT treatments using KUR (Kyoto University Research Reactor) were adapted for malignant melanoma and brain tumors. The widespread application to the treatment of other diseases such as recurrent head and neck tumors, liver tumors (Suzuki et al., 2007), and mesothelioma (Suzuki et al., 2006) using epithermal neutrons, has resulted in an increased number of clinical trials. In order to obtain good results for deep tumors, a higher dose is required. Moreover, a sufficient neutron yield obtained by using an accelerator-based neutron source that can be located near a hospital would be useful for further developments of BNCT.

Yonai et al. (2003) and Tahara et al. (2006) are already investigating a neutron source using spallation reactions that occur for 30–50 MeV protons incident on a tantalum target. The possibility of exploiting the reaction of several tens of MeV protons incident on a beryllium target, was excluded because of the fast neutrons contamination of the treatment beam. However, a sufficient epithermal neutron yield based on the Be(p,n) reaction could be obtained with an optimum beam-shaping assembly. Our system has the advantage of a larger neutron yield and a lower activation of the target material in comparison with the spallation reactions involving heavy materials.

The neutron transport for optimum treatment beams was simulated by using the Monte Carlo calculation code MCNPX (Pelowitz, 2005). This article reports an overview of the epithermal neutron generator and calculated parameters in phantom.

2. Material and methods

2.1. Cyclotron accelerator and beryllium target

The cyclotron accelerator (HM-30) manufactured by Sumitomo Heavy Industries is employed to provide a ~1 mA, 30 MeV proton beam. In the HM-30 hydrogen negative ions are accelerated and protons up to 30 MeV are derived by charge conversion in a carbon

* Corresponding author.
E-mail address: h-tanaka@rri.kyoto-u.ac.jp (H. Tanaka).

0969-8043/$ - see front matter © 2009 Elsevier Ltd. All rights reserved.
doi:10.1016/j.apradiso.2009.03.096

Table 1
Target material properties for Be, Ta and W.

Target	Melting point (deg)	Boiling point (deg)	Thermal conductivity ($W m^{-1} K^{-1}$)	Neutron yield ($sec^{-1} mA^{-1}$)	Gamma ray yield per one neutron
Be	1278	2970	201	1.90×10^{14}	0.02
Ta	3017	5458	57.5	1.27×10^{14}	0.93
W	3422	5555	174	9.65×10^{13}	1.40

foil stripper. The proton beam derived from HM-30 is led to a beryllium target via a beam transport system. A uniform 120 mm × 120 mm proton beam at the beryllium target is shaped by a controlling magnetic field of two scanning magnets.

Table 1 shows the characteristics of Be, W, and Ta target materials when irradiated by a 1 mA, 30 MeV proton beam. The neutron and gamma ray yields were estimated by using the MCNPX code and the cross-section data of ENDF/B-VII, physical model, and la150 for Be, Ta, and W, respectively. In comparison with the other materials listed in Table 1, Be shows the highest neutron yield, the smallest gamma-ray yield per neutron, the highest thermal conductivity, and a high melting point. A 1 mA, 30 MeV proton beam has a 30 kW power. Such a large heat input needs a target-cooling system. In our system, a Be target is directly cooled by pure compressed water. The compressed water flows through a spiral water channel. 30 MeV protons with a range of 5.8 mm in Be penetrate a 5.5 mm-thick Be target and inject in the compressed cooling water in order to prevent blistering of the target.

With regard to the experimental results for the thermal resistance of a Be target, Tadokoro et al. (2006) indicated that a heat input of 500 W/cm^2 leads to a temperature less than 500 °C. The irradiation area should be expanded to 60 cm^2 for a heat input of 500 W/cm^2 under 30 kW operation. The area of 144 cm^2 scanned by two scanning magnets is sufficient for heat reduction on the target.

In order to evaluate the target activation resulting from 1 year of operation a 2 h irradiation per day with a 1 mA proton current was assumed. The neutron- and proton-induced activation of the three above materials was calculated by using the IRACM code (Tanaka et al., 1997). The nuclei produced in a W target have higher activity and longer half lives than Be and Ta targets. Immediately after the daily operation, the activation rate of a Ta target is four orders of magnitude higher than that of a Be target. The period required for the Ta target until the ambient dose rate becomes 1 $mSv h^{-1}$ is twice of that required for the Be target. Considering the above-mentioned results in terms of neutron yield, thermal properties, and activation level, the Be target was chosen.

2.2. Beam-shaping assembly (BSA)

Yanch et al. (1991) found out that for BNCT treatments at a 10 cm depth in the head, the most effective neutron energy is 10 keV and the most effective neutron energy range is between 4 eV and 40 keV.

In the reaction between 30 MeV protons and a Be target, the neutrons that are emitted in the forward direction have an energy of up to 28 MeV. In order to reduce the neutron energy to the epithermal energy range, a BSA composed of a moderator and a shaper has been employed. The moderator is used to reduce the energy from the maximum value of 28 MeV with low capture cross-section. The shaper is used to obtain the 10 keV optimum energy mentioned above.

Fig. 1 shows the schematic layout of the BSA. The moderator materials are Pb and Fe. The Pb component, used as a breeder and a reflector for high energy neutrons, was installed near the target.

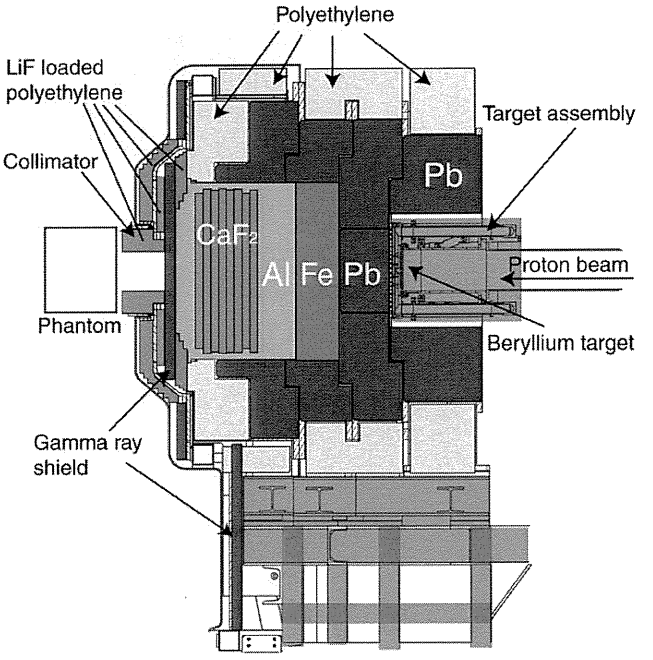

Fig. 1. Schematic layout of the BSA to obtain an epithermal neutron beam using a 30 MeV proton beam incident on a beryllium target.

The Fe component, mainly used as a moderator, was installed after the Pb component. With regard to the shaper, AlF_3 is often used in the design of an epithermal neutron generator (Liu et al., 2004; Culbertson et al., 2004) and the material density should be high in order to form a compact BSA. It is difficult to increase the AlF_3 density because it sublimes at a temperature of 1040 °C under atmospheric pressure. Therefore, we focused on Al and CaF_2 instead of AlF_3.

The optimum thickness of each component was determined through the calculation of the dose distribution in the phantom composed of soft average tissue of an adult male (ICRU-44) by using the MCNPX code.

In order to prevent the exposure of the patient to the fast-neutron radiation, the moderator, the shaper, and the front surface of the collimator are surrounded by polyethylene blocks.

Furthermore, in order to accurately set the patient in the position determined by the treatment planning system, an X-ray tube and an imaging plate are installed. The pair of X-ray tube and imaging plate can be moved to the neutron beam side and an image of the "beam's eye view" can be obtained. Laser markers are also installed; the irradiation position is set by a marking on the skin.

3. Results and discussion

All the following results are related to a 1 mA, 30 MeV proton beam.

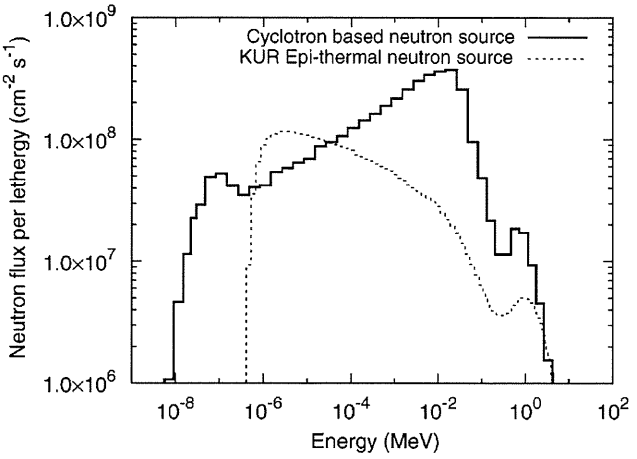

Fig. 2. Comparison between the CBNS neutron spectrum and the KUR one.

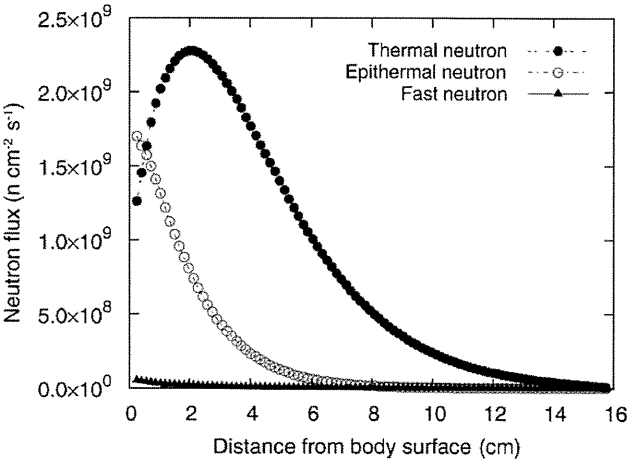

Fig. 3. Neutron flux components (thermal, epithermal and fast) in phantom.

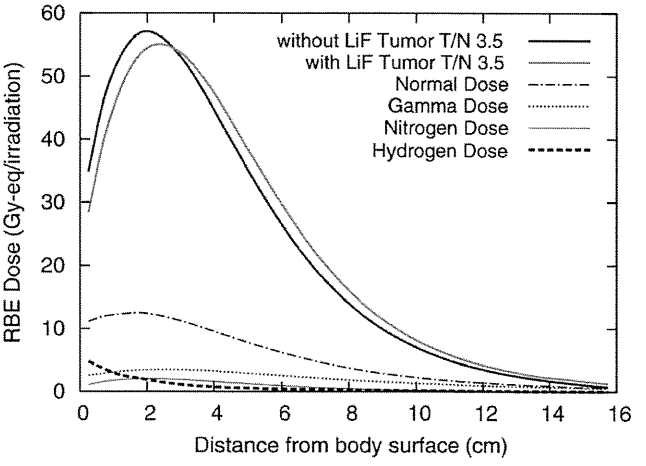

Fig. 4. RBE dose components in phantom.

3.1. Free beam properties

Fig. 2 shows the CBNS neutron flux spectrum under the free-air condition evaluated at the surface of the gamma-ray shield in comparison with the KUR one, which is most-often used in the BNCT treatments (Sakurai and Kobayashi, 2000). The CBNS neutron spectrum has a peak in the 10–20 keV energy range.

In some of the BNCT literature, the epithermal range is defined as the interval from 0.5 eV to 10 keV, which is recommended by IAEA-TECDOC1223 (2001). However, we designed the moderator to fulfill the maximization of epithermal neutron flux with the interval from 4 eV to 40 keV, which is more effective to treat deep tumors. Furthermore, Blue et. al. (1993) showed the calculated RBE value as a function of neutron energy and found out that the RBE of the energy of 40 keV was less than 3.0. They also showed the RBE of the energy of around 0.5 eV was less than 3.0. It is appropriate to define the value of 40 keV as boundary energy between epithermal and fast neutron. Consequently, in this article, the definition of the epithermal energy range is from 0.5 eV to 40 keV. The energy region below 0.5 eV is defined as the thermal region; that above 40 keV, as the fast-neutron region.

The fast-neutron and gamma-ray dose contaminations per epithermal neutron for CBNS under the free-air condition are 5.84×10^{-13} and 7.75×10^{-14} Gy cm^2, respectively. Each absorbed dose value was obtained by using the neutron flux at the gamma-ray shield and the flux-to-dose conversion factors published in ICRP-74. The human tissue components were assumed to be H: 11.1, C: 12.6, N: 2.0, and O: 74.3 (wt%). The fast-neutron and gamma-ray dose contaminations per epithermal neutron for KUR under the free-air condition are 9.10×10^{-13} and 2.40×10^{-13} Gy cm^2, respectively (Sakurai and Kobayashi, 2000). With regard to the fast neutrons and gamma rays contaminations the CBNS facility is superior to KUR one.

3.2. Beam characteristics in phantom

Fig. 3 shows the evaluation of the CBNS neutron flux components in a phantom located in front of the collimator. The diameter of the collimator aperture and phantom are 16 and 26 cm, respectively. The maximum value of thermal neutron flux is 2.3×10^9 cm^{-2} s^{-1} at a depth of 2.3 cm in phantom.

The prescribed dose is determined by the differential boron accumulation in tumor and normal cells (T/N ratio) and the boron concentration in the blood of the patient. The RBEs assumed for nitrogen, hydrogen, and gamma rays are 3.0, 3.0, and 1.0, respectively. The compound biological effectiveness (CBE) factors for tumor and normal brain are 3.8 and 1.35, respectively. The T/N ratio of 3.5 is employed. The boron concentration is assumed to be 13 ppm. The therapeutic time is determined by the dose limit for the normal brain of 12.5 Gy-eq. Fig. 4 shows the distribution of the RBE dose components in the phantom. Under the above hypotheses, the RBE dose in tumor reaches a maximum value of 57 Gy-eq at a depth of about 2.3 cm in phantom and the irradiation time is less than 30 min. The sufficient dose for killing the tumor is at least 30 Gy-eq. The CBNS facility can treat a tumor located within a depth of 5.5 cm, with the RBE dose of 30 Gy-eq by single irradiation. With regard to the irradiation of deeper tumors, the bilateral irradiation can be adopted to raise the prescribed dose. At a depth of 8 cm, the RBE dose is about 15 Gy-eq. Therefore CBNS can treat tumors situated at almost all the positions in the brain by using the bilateral irradiation.

Furthermore, to improve the dose distribution at a deeper position, an enriched ^{6}LiF ceramic filter (thickness of 6 mm) placed after the gamma ray shield can be used. The enriched ^{6}LiF filter produces a more ideal neutron spectrum because of filtering in the low energy region. The thickness of ^{6}LiF filter is optimized to fulfill a therapeutic time of less than 60 min. Fig. 4 shows the dose distribution in phantom using the enriched ^{6}LiF ceramic

filter. The use of this filter increases the treatable depth from 5.5 to 6.0 cm with the RBE dose of 30 Gy-eq.

4. Conclusions

By means of Monte Carlo simulations a moderator and a shaper have been optimized for the high energy neutrons emitted from the Be(p,n) reaction with a 1 mA, 30 MeV proton beam. With regard to the fast neutrons and gamma rays dose contamination, CBNS is superior to the current KUR facility. From the evaluation of the dose distribution in a phantom the irradiation time using CBNS turns out to be about 30 min. CBNS becomes a powerful tool for treating deep tumors by using the bilateral irradiation. The CBNS facility is now under construction and the aim is to establish it at KURRI by 2009. KUR also will restart in the middle of 2009. Thus KURRI will have both the reactor- and the accelerator-based neutron sources for BNCT.

References

Blue, T.E., Gupta, N., Woollard, J.E., 1993. A calculation of the energy dependence of the RBE of neutrons. Phys. Med. Biol. 38, 1693–1712.

Culbertson, C.N., Green, S., Mason, A.J., Picton, D., Baugh, G., Hugtenburg, R.P., Yin, Z., Scott, M.C., Nelson, J.M., 2004. In-phantom characterisation studies at the Birmingham accelerator-generated epithermal neutron source (BAGINS) BNCT facility. Appl. Radiat. Isot. 61, 733–738.

IAEA TECDOC 1223, 2001. Current status of neutron capture therapy.

Liu, Y.W.H., Huang, T.T., Jiang, S.H., Liu, H.M., 2004. Renovation of epithermal neutron beam for BNCT at THOR. Appl. Radiat. Isot. 61, 1039–1043.

Pelowitz, D.B., 2005. MCNPX user's manual—version 2.5.0. Los Alamos National Laboratory Report LA-CP-05-0369.

Sakurai, Y., Kobayashi, T., 2000. Characteristics of the KUR heavy water neutron irradiation facility as a neutron irradiation field with variable energy spectra. Nucl. Instrum. Methods A 453, 569–596.

Suzuki, M., Sakurai, Y., Masunaga, S., Kinashi, Y., Nagata, K., Maruhashi, A., Ono, K., 2006. Feasibility of boron neutron capture therapy (BNCT) for malignant pleural mesothelioma from a viewpoint of dose distribution analysis. Int. J. Radiat. Oncol. Biol. Phys. 66 (5), 1584–1589.

Suzuki, M., Sakurai, Y., Hagiwara, S., Masunaga, S., Kinashi, Y., Nagata, K., Maruhashi, A., Ono, K., 2007. First attempt of boron neutron capture therapy (BNCT) for hepatocellular carcinoma. Jpn. J. Clin. Oncol. 37 (5), 376–381.

Tadokoro, T., Kawakubo, Y., Seki, H., Tayama, R., Umegaki, K., Baba, M., Kobayashi, T., 2006. Feasibility study on a common use accelerator system of neutron production for BNCT and radionuclide production for PET. Advances in neutron capture therapy 2006. In: Proceedings of ICNCT-12, pp. 304–307.

Tahara, Y., Oda, Y., Shiraki, T., Tsutsui, T., Yokobori, H., Yonai, S., Baba, M., Nakamura, T., 2006. Engineering design of a spallation reaction-based neutron generator for boron neutron capture therapy. J. Nucl. Sci. Technol. 43 (1), 9–19.

Tanaka, S., Fukuda, M., Nishimura, K., 1997. A code system to calculate induced radioactivity produced by ions and neutrons. JAERI-Data/Code 97-019.

Yanch, J.C., Zhou, X.L., Brownell, G.L., 1991. A Monte Carlo investigation of the dosimetric properties of monoenergetic neutron beams for neutron capture therapy. Radiat. Res. 126, 1–20.

Yonai, S., Aoki, T., Nakamura, T., Yashima, H., Baba, M., Yokobori, H., Tahara, Y., 2003. Feasibility study on epithermal neutron field for cyclotron-based boron neutron capture therapy. Med. Phys. 30 (8), 2021–2030.

РОССИЙСКИЙ ФИЗИОЛОГИЧЕСКИЙ ЖУРНАЛ им. И. М. СЕЧЕНОВА

RUSSIAN JOURNAL OF PHYSIOLOGY
(formerly I. M. Sechenov Physiological Journal)
95 · N 12 · 2009

THE ROLE OF IMMUNE CELLS IN BRAIN METASTASIS OF LUNG CANCER CELLS AND NEURON-TUMOR CELL INTERACTION

© M. Noda, T. Seike, K. Fujita,[3] Y. Yamakawa, M. Kido,[1] H. Iguchi[2]

[1] Laboratory of Pathophysiology, Graduate School of Pharmaceutical Sciences,
[2] Laboratory of Anatomy and Cell Biology, Graduate School of Dental Sciences,
Kyushu University, Fukuoka, JAPAN,
[3] Shikoku Cancer Center Research Institute, Ehime, JAPAN

Following any type of brain injury such as lesion, stroke, and tumor/cancer invasion, microglia are rapidly activated and recruited to the site of injury. Microglia is the main immune effector cell population of the central nervous system and control immune cell recruitment. However, the molecular mechanism of brain metastasis and interaction between neuron-glia-tumor cells are poorly understood. Therefore, we established an animal model for brain metastasis using human lung cancer-derived cells (HARA-B) in nude mice. Accumulation of activated microglia was observed around tumor cells depending on the size of metastatic foci and the area of the brain. *In vitro* study, conditioned medium from primary cultured mouse microglia inhibited the proliferation of tumor cells, while tumor cell-conditioned medium inhibited the proliferation of primary cultured neurons from mouse cortex. Though the responsible factors released from microglia and tumor cells are still under investigation, these studies will contribute to understand the mechanism of cell-cell interaction in the brain and possible therapeutic target for brain metastasis.

Key words: immune cells, brain, cancer, cell interaction.

RUSSIAN JOURNAL OF PHYSIOLOGY, V. 95, N 12, P. 1386—1396, 2009

INTRODUCTION

The probability of metastasis is dependent on the tumor cell phenotype including the invasive, adhesive and growth ability, and interaction between the tumor cell and the organ environment, such as the cellular components, cytokines, organ-derived growth factors [15]. Brain metastases from lung cancer occur with higher incidence as well as from breast cancer. In pathological studies the occurrence of brain metastases is between 30 and 50 % of total case of non-small lung cancer (NSCLC) [6, 11, 13]. The reason for high frequency of brain metastases may be that the brain microenvironment plays an important role in the progression of lung or breast cancer cells in the brain.

In the brain, microglial cells are considered as the pathologic response element [10, 12]. Microglial cells are dispersed throughout the entire central nervous system (CNS) and exhibit a ramified morphology under normal conditions. As recently shown by Davalos et al. [4], and Nimmerjahn et al. [16], microglial processes are highly dynamic in the intact brain, suggesting that microglial cells scan the brain parenchyma with their processes and potentially shield it from injury. Under pathologic conditions such as a lesion, stroke, neurodegenerative disorders or tumor invasion, activated microglia migrate rapidly to the affected sites of the CNS. At the same time, microglial activation

is accompanied by the release of immunocompetent molecules such as cytokines or chemokines, and other substances such as growth factors [7].

Activated glial cells contribute to a part of the innate immune response in the brain and produce a large variety of different mediators of inflammatory reaction [1]. Therefore, we investigated interaction between tumor cells and glia or neurons. Our results may help understand the mechanism of brain metastases and may contribute to a new therapeutic strategy to prevent or attenuate brain metastases.

MATERIALS AND METHODS

Animal model for brain metastasis

Male 5-week-old BALB/c *nu/nu* mice (Kyudo, Kumamoto, Japan), kept in specific pathogen-free environment, were used. A single suspension of HARA-B cells (2×10^5 cells/0.2 ml PBS) was inoculated into the left ventricle of the nude mice according to the method described previously [6]. Then, mice were subjected for *in vitro* experiments 4 to 5 weeks after cell inoculation.

Immunohistochemistry

Nude mice were perfused transcardialy with 50 ml of 10 U/ml and 0.5 % procaine in PBS and 4.0 % paraformaldehyde in PBS. Then, the brain was removed and post-fixed for 3 hour, cryoprotected for 24 hour in PBS containing 20 % sucrose. The brain was sliced into 20 μm in thickness by using a cryostat and the sections were placed on a slide glass pre-coated with gelatin, permeabilized with 0.3 % TritonX-100 in PBS for 15 min and blocked in PBS containing 1 % BSA and 5 % normal donkey serum (Jackson Immuno Research) for 1 hour at room temperature. Then, brain sections were incubated over night at 4 °C with primary antibodies, including FITC-conjugated anti-human cytokeratin antibody (CAM5.2) (Becton Dickinson, undiluted solution) and or rabbit anti-Iba1 antibody (Wako Chemicals, 1:500). The secondary antibody for Iba-1 was Cy3-conjugated donkey anti-rabbit IgG (1:250). Every treatment was followed by washing three times for 5 min with PBS containing 0.3 % TritonX-100. Sections were mounted in the Perma Fluor Aqueous Mounting Medium (Thermo, Shandon, Pittsburgh, PA) and were analyzed with a confocal microscope (LSM510 META, Carl Zeiss, Co. Ltd. Germany).

Cell culture

The study was approved by the Animal Research Committee of Kyushu University, and carried out in accordance with the National Institutes of Health Guide for the Care and Use of Laboratory Animals.

Primary glial cell cultures were obtained from cerebral cortex of 1-day-old C57BL/6 mice (Kyudo, Kumamoto, Japan). The cortex was isolated under a dissecting microscope and carefully separated from the choroid plexus and meninges. The cerebral cortex was minced and treated with trypsin-EDTA solution (0.25 % trypsin, 1 mM EDTA and 1500 U DNase in HBSS) at 37 °C for 10 min. Cell suspensions were filtered through 70 μm pore size mesh (BD Falcon, USA) into Dulbecco's modified Eagle medium (DMEM; Nissui, Tokyo, Japan) containing 10 % fetal calf serum (FCS, Hyclone, UT, USA), 2 mM L-glutamine, 100 U/ml penicillin, 100 μg/ml streptomycin, 0.37 % $NaHCO_3$, 110 μg/ml pyruvic acid. After centrifugation, cells were filtered through 40 μm pore size mesh (BD Falcon, Bedford, MA, USA) and plated into 75 cm^2 cell culture flask at density of 10^7 cell/75 cm^2 and maintained at 37 °C in 10 % CO_2-90 % air with change of medium twice per week.

Microglial cells were first obtained after 10—14 days of mixed glial cell cultures, and then every 1 week, from the surface of the mixed primary cultured cell layer by gently shaking the flasks for 20 min. The resulting cell suspension was seeded onto glass coverslips and allowed to adhere for 30 min at 37 °C. Then, microglial cells were isolated as strongly adhering cells after

unattached cells were removed. The purity of microglia as measured with the isolectin technique, ranged from 95—99 %.

Neuronal cell cultures were prepared from cerebral cortices of embryonic day 14—16 (E14—16) C57BL/6 mice brains. The cortices were trypsinized together with DNase1 and dissociated with a fire-polished pipette and washed twice. Cells were plated on 4-well culture slides (BD Falcon, Bedford, MA, USA) that had been previously coated overnight with poly-D-lysine (50 μg/ml, Sigma) and incubated in culture medium (high-glucose DMEM, GIBCO) supplemented with 110 μg/ml pyruvic acid, 3.7 mg/ml $NaHCO_3$, 5 μg/ml insulin, 2 mM L-glutamine, 100 units/ml penicillin, 100 μg/ml streptomycin, 2 % B27 supplement (GIBCO). Cells were used after 7 days. The density of neuronal cells was about 5×10^4 cell/well.

HARA-B cells were maintained in the medium mentioned above at 37 °C in 10 % CO_2-90 % air. Cells were grown as a monolayer culture in 25 cm^2 cell culture flask (Nalge Nunc International), and single-cell suspension of cells was obtained by trypsin treatment.

Cell proliferation assay

In co-culture experiment, HARA-B cells (0.5×10^3 cells/well) and microglia or neurons (2.5×10^3 or 5×10^3 cells/well) were seeded into 8-well cell culture slide (BD Falcon) with DMEM for 24 hour. Then, cells were rinsed twice with PBS and incubated in serum free DMEM. After 72 hour of co-culture, cells were fixed with 4% paraformaldehyde for 30 min at room temperature and permeabilized with 0.3 % TritonX-100 in PBS for 15 min and blocked in PBS containing 1 % BSA and 5 % normal donkey serum (Jackson Immuno Research) for 1 hour at room temperature. Cells were incubated with primary antibody of monoclonal mouse anti-human cytokeratin antibody (AE1/AE3 pool of cytokeratin) (Dako, 1:100) over night at 4 °C, followed by incubated for 5 hour at room temperature with secondary antibody of FITC-conjugated anti-mouse IgG (Sigma, 1:500) and then for 30 min at room temperature with 300 nM 4′, 6′-diamidino-2-phenylindole hydrochloride (DAPI, Sigma). Numbers of all HARA-B cells in a well were counted by using a digital camera system (Axio Cam, Carl Zeiss) mounted on a light and fluorescent microscope (Axopscope2 plus, Carl Zeiss). The results were indicated as the percentage of control (single cell culture of HARA-B cells). The glial cell-conditioned medium was obtained by culturing mice primary cultured microglia or astrocytes at a density of 10^4 cells/well for 72 hours. The medium was removed, centrifuged at 2000 rpm for 10 min and then added to the well of HARA-B cell culture at the volume of 25 or 50 %. The number of HARA-B cells were counted as mentioned above.

TUNEL staining and BrdU staining

In situ cell death detection kit (Roche Applied Science) was used for TUNEL staining according to the protocol provided by the manufacturer. BrdU (Roche Applied Science, 10 μM) was added to microglial culture medium for 24 h, fixed with 4 % paraformaldehyde, denaturation of DNA by acid, and stained with anti-BrdU antibody (Santa Cruz, 1:200) with Alexa568-conjugated anti-mouse IgG (1:500) as a secondary antibody.

Statistical analysis

One-way analysis of variance (ANOVA) and post-hoc Bonferroni/Dunn test were used to examine the statistical differences. Differences were considered significant at $^*p < 0.05$ and $^{**}p < 0.01$.

RESULTS

Microglial cells around metatatic region

To investigate the interaction between tumor cells and microglia, an experimental model for brain metastasis using human lung cancer-derived cells (HARA-B cells) was established. Cancer cells (HARA-B cells) metastasized to whole region of the brain, especially cortex, 4—5 weeks af-

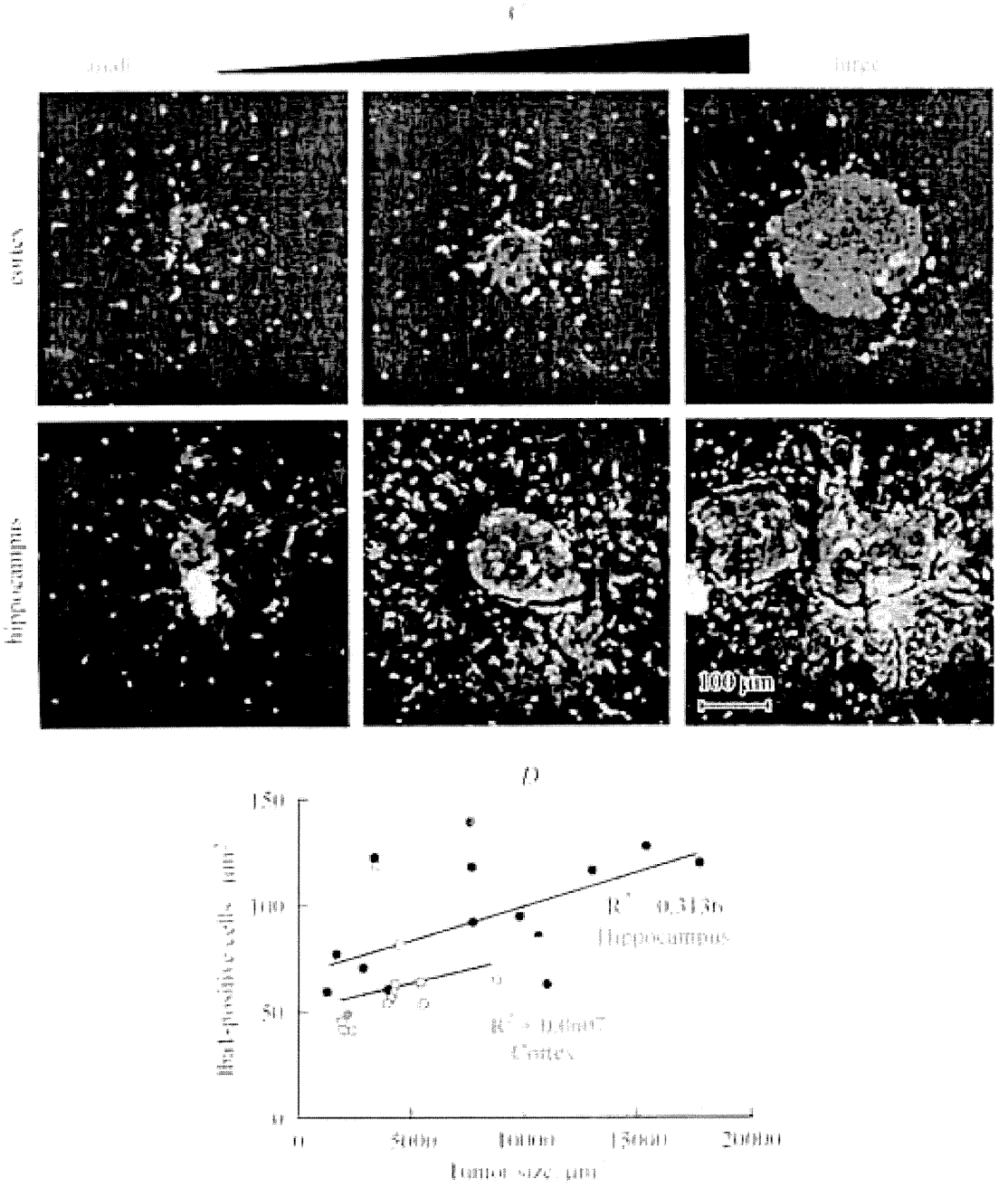

Fig. 4 Microglia accumulates around HARA-B cells *in vivo*

C — typical example of microgliosis around the tumor, and microglia accumulate in relation to the size of the metastatic foci. *D* — correlation between tumor size and microgliosis. Number of Iba1-positive cells were counted. Z-stack images were obtained from each section (30 μm thickness) by LSM 510 Meta (Carl Zeiss). *C'* — typical examples showing that more microglia accumulated around metastatic foci in hippocampus than in cerebral cortex. *D'* — correlation between tumor size and Iba1 in hippocampus and cortex.

ter intracardiac inoculation. In brain slices obtained from normal and tumor-bearing mice, cancer cells and microglia/macrophage were stained with anti-cytokeratin antibody and anti-Iba1 antibody, respectively. At 3 weeks after the inoculation of HARA-B cells into cardiac ventricle, metastatic foci were found in midbrain-lateral cortex (data not shown). At 4—6 weeks, metastatic foci of various sizes were found throughout the brain. Bigger metastatic foci attracted more microglia

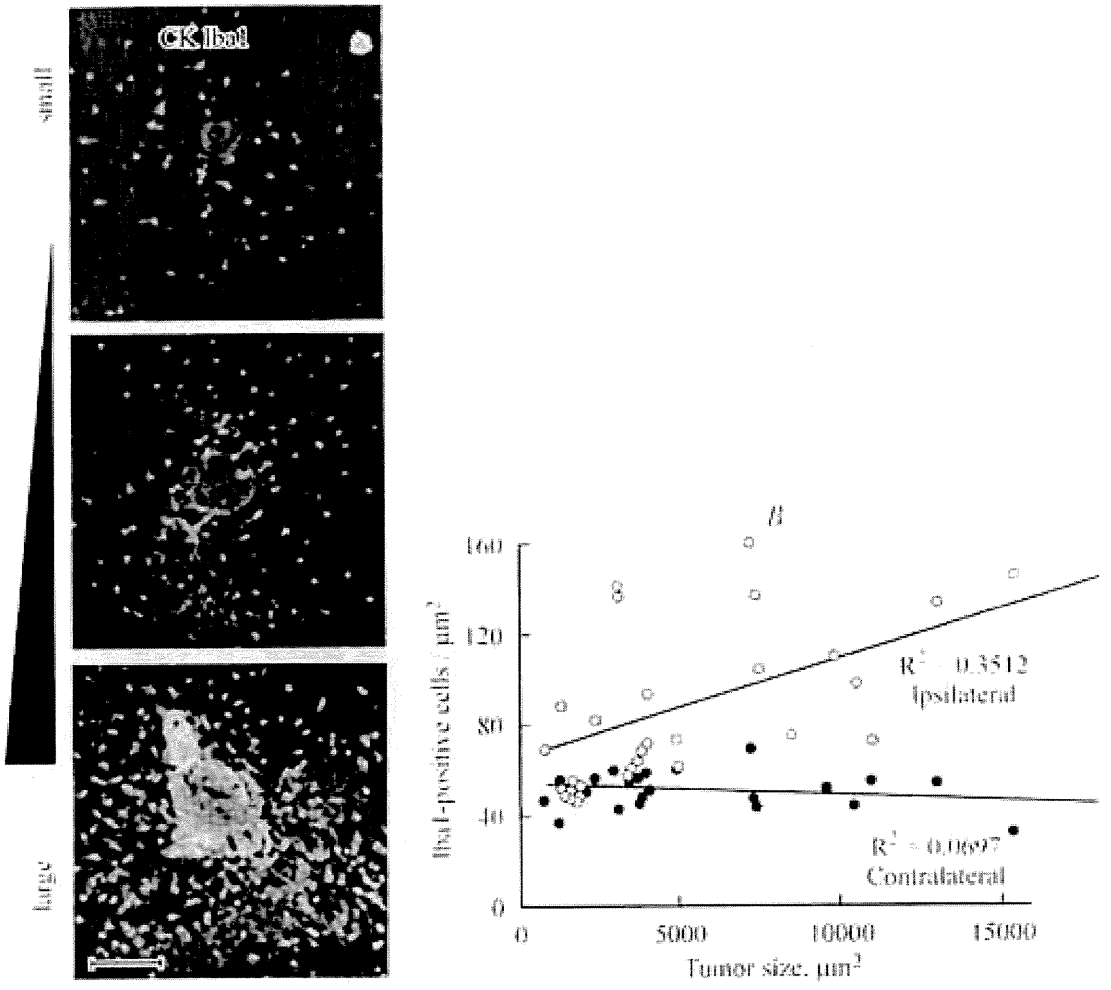

Fig. 1 (*continuation*).

(Fig. 1, *A*), with the correlation factor of tumor size and Iba1 intensity of 0.351 (Fig. 1, *B*). Though the incidence of brain metastasis was different depending on each mouse, the highest incidence was generally observed in cerebral cortex and hippocampus (Fig. 1, *C*). The correlation factor of tumor size and Iba1 intensity was higher in hippocampus (0.314) than that in cortex (0.061) (Fig. 1, *D*).

Effects of microglial cells on proliferation of cancer cells

To investigate the effects of microglia on the proliferation of cancer cells, the interaction between HARA-B cells and microglia *in vitro* was examined. First, HARA-B cells were co-cultured with primary cultured mouse microglia for 3 days and compared the proliferation of HARA-B cells. In the condition of co-culture with microglia with the ratio of 1:5 and 1:10 (cancer cells:microglia), the relative number of HARA-B cells was attenuated to 62.8 ± 3.8 % ($p < 0.05$, $n = 4$) and 41.7 ± 2.3 % ($p < 0.01$, $n = 4$), respectively, compared to the one without microglia (control, 100 %) (Fig. 2, *A*).

Next, to elucidate whether the inhibitory effect of microglia was due to the physical contact or some effects of conditioned medium obtained from microglial cell cultures on the proliferation of HARA-B cells were examined. In the presence of 25 and 50 % of microglia-conditioned medium (MCM) in the total volume of HARA-B cell culture-medium, the proliferation of HARA-B cells

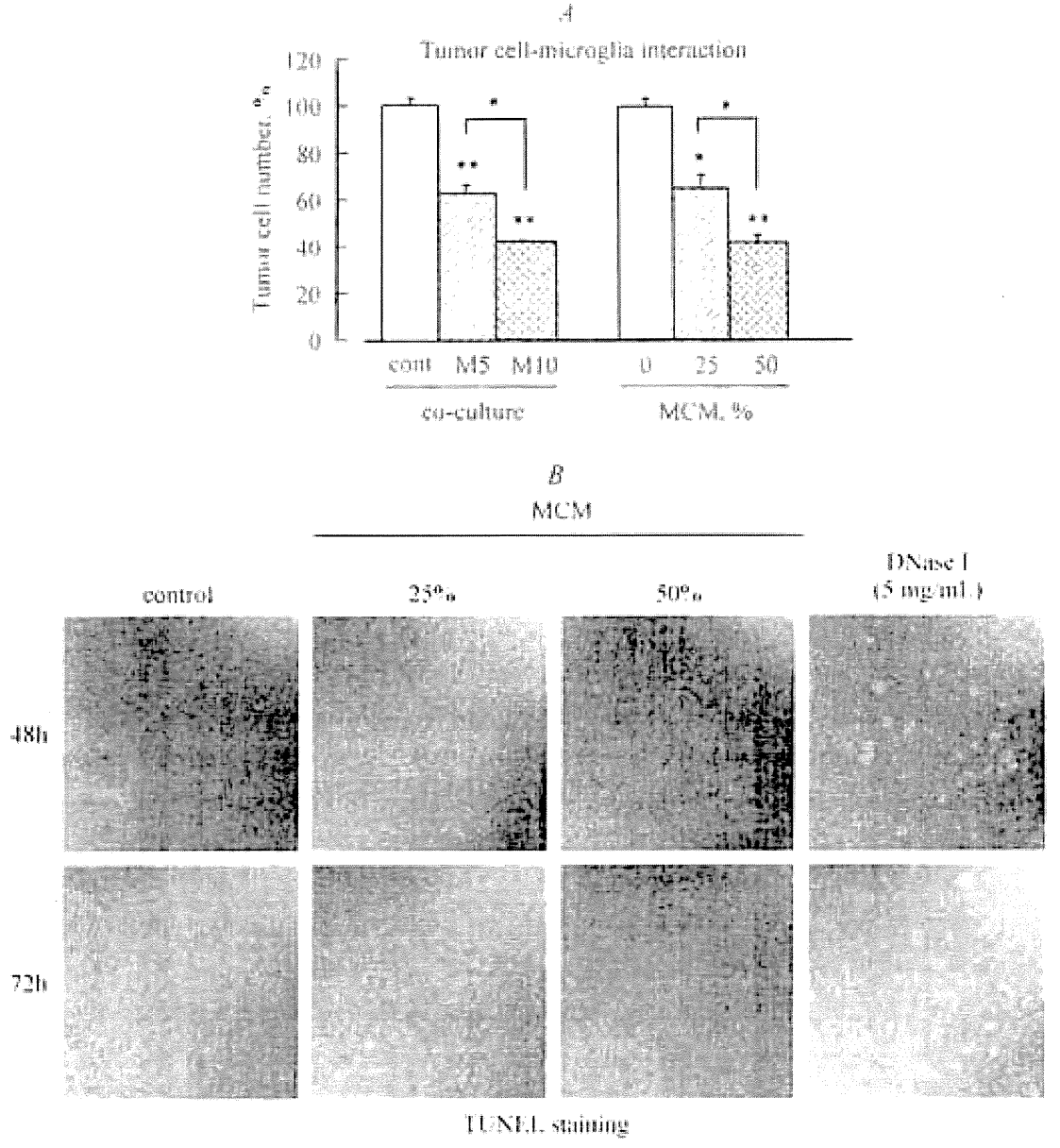

Fig. 2. Effects of co-culture or conditioned medium of microglia on the proliferation of tumor cells.

A — co-culture of tumor cells (HARA-B cells) and mouse primary cultured microglia (HARA-B: microglia, 1 : 5 or 1 : 10) and addition of microglia-conditioned medium (MCM; 25 or 50 % of total volume) inhibited the proliferation of cancer cells; *B* — TUNEL staining of HARA-B cells with or without (control) 25 or 50 % MCM after incubation for 48 and 72 h. Addition of DNase I shows positive control; *C* — BrdU staining of HARA-B cells with or without (control) 25 or 50 % MCM. * $p < 0.05$. ** $p < 0.01$.

was attenuated to 65.9 ± 6.1% ($p < 0.05$, $n = 5$) and 42.6 ± 2.1 % ($p < 0.01$, $n = 5$), respectively, compared to that in the absence of MCM (control; 100 %) (Fig. 2, *A*). These values were similar to those observed in the co-culture experiments.

To elucidate the mechanism on how microglia suppress the proliferation of HARA-B cells, first the apoptosis staining, terminal deoxynucleotidyl transferase-mediated dUTP-biotin nick end labeling (TUNEL) staining, was performed. No significant TUNEL staining was observed in HARA-B cells with 25 or 50 % of MCM for 48 or 72 h incubation (Fig. 2, *B*). Next, 5-bromo-2'-deoxyuridine (BrdU) staining were performed to detect cells that were actively replicating

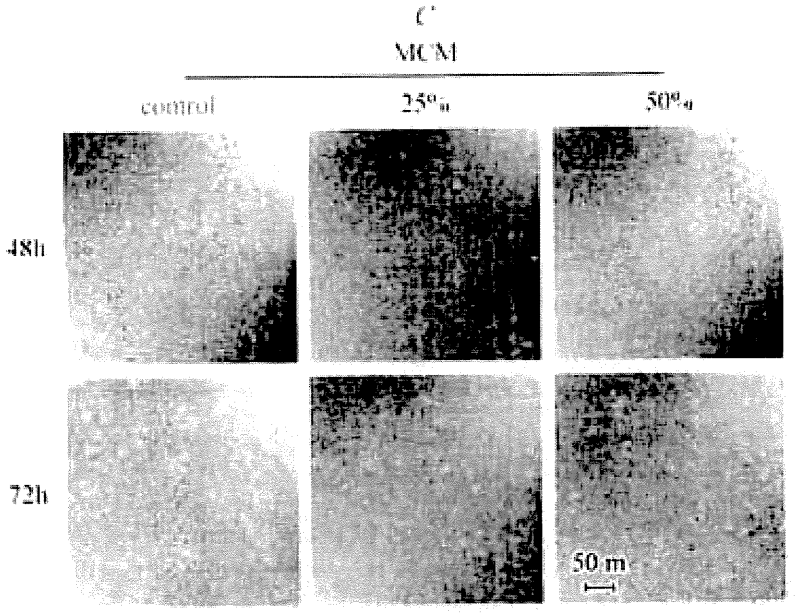

Fig. 2 (*continuation*).

their DNA. There was apparent and time-dependent decrease in BrdU-positive HARA-B cells with 25 or 50 % of MCM (Fig. 2, *C*). These results suggest that the inhibition of HARA-B cell proliferation may due to cell-cycle arrest but not apoptosis.

Interaction between neurons, tumor cells and microglia

Since cavities were often observed around metastatic foci, neuronal damage by tumor cell proliferation was speculated. In order to elucidate the relationship between neurons and tumor cells, the effects of co-culture of HARA-B cells and primary cultured neurons from mouse cerebral cortex were investigated. As speculated, addition of HARA-B cells inhibited the survival of neurons depending on the number of HARA-B cells (Fig. 3, *A*). Though the mechanism of tumor-induced inhibition of neuronal survival is not known, the inhibitory effects of HARA-B cells on neuronal survival were further analyzed by adding microglial cell. Since microglia inhibited the proliferation of HARA-B cells, microglia could rescue the neuronal survival. Addition of microglia to neurons did not show any significant effects, assessed by counting MAP2-positive cells. However, when microglia was added to co-culture of neurons with HARA-B cells, the disturbed neuronal survival partially recovered (Fig. 3, *B*). Fig. 3, *C* shows the semi-quantitative analyses on the number of MAP2-positive cells. These results suggest that microglia have neuroprotective role on tumor-induced neuronal damage.

DISCUSSION

Certain cancers, i. e. breast cancer and lung cancer, are liable to metastasize in the brain. The incidence of the brain metastasis has been increasing in recent years [17]. In the metastatic process, the microenvironment of the metastatic sites plays an important role for tumor cells to invade and proliferate in the target tissues [5]. Such a microenvironment contains many resident cell types in addition to tumor cells as well as migratory hematopoietic cells. In bone metastasis, for example, tumor cell-bone cell interaction disrupts normal bone remodeling through physical and/or soluble contact, which results in bone destruction or new bone formation [19]. It is important to elucidate the molecular mechanism, as a lead toward developing a molecular target therapy. In fact, a humanized monoclonal antibody against the receptor activator of NF-κB ligand (RANKL), which plays

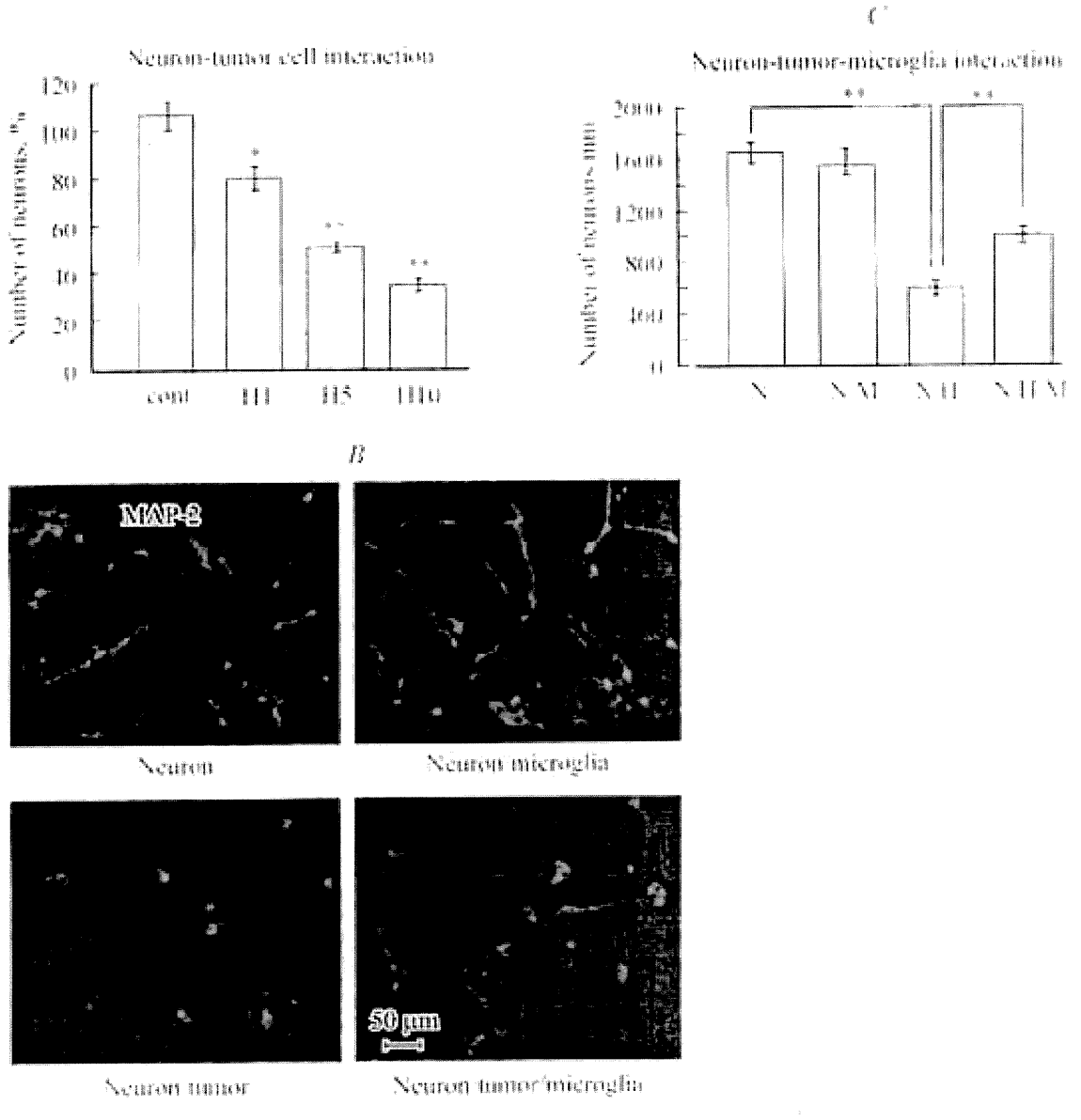

Fig. 3. Tumor cells inhibited neuronal survival but was partially recovered by addition of microglia *in vitro*.

A – the number of primary cultured neurons from mouse cerebral cortex was inhibited by co-culture with HARA-B cells (neurons: HARA-B cells, 1 : 1, 1 : 5 and 1 : 10); *B* – fluorescent images of MAP2-positive neurons with or without HARA-B cells and/or microglia; *C* – the number of neurons was analyzed semi-quantitatively. N: neurons, H: HARA-B cells, M: microglia.

a crucial role in the formation of bone metastasis [14], has been generated, and a phase III trial for this monoclonal antibody is under way as a potential treatment for bone metastasis [1].

With regard to brain metastases, such an interaction of tumor cells with other cells in the brain microenvironment is unclear, and available information is limited to date. In the present study, histological examination revealed that activated astrocytes accumulated around the metastatic foci of HARA-B cells in the brain, and their number increased during the progression of brain metastasis. Similarly, accumulation of astrocytes around brain metastases was also observed in autopsy cases [3]. Such observations, together with the histological findings in the present study, suggest that astrocytes, accumulated around the brain metastasis, interact with metastatic tumor cells and create a favorable microenvironment for tumor cells in the brain.

In the present study, in the animal model of brain metastasis using human lung cancer-derived cells (HARA-B cells), large number of activated microglia, and also macrophages presumably in-

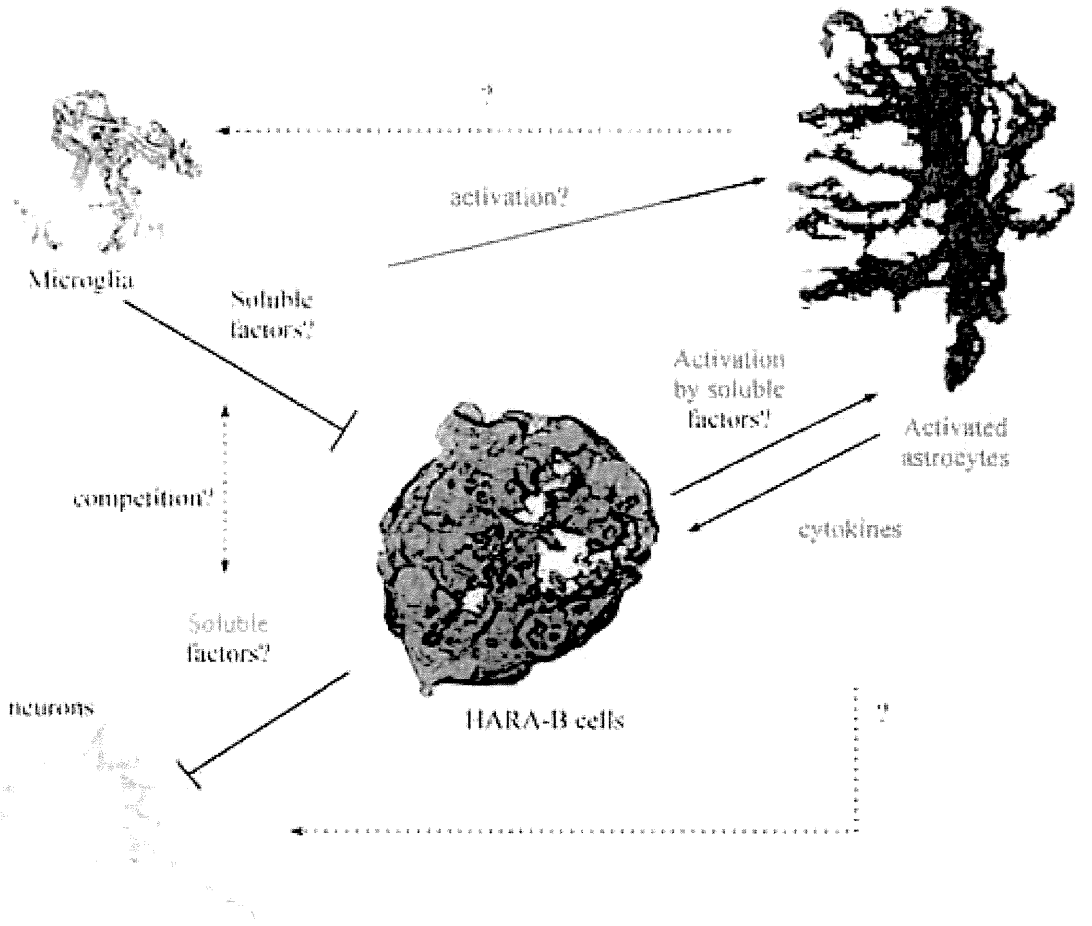

Fig. 4 Proposed schema on neuron-glia-tumor cell interactions. Microglial cells release some soluble factors and suppress the proliferation of tumor cells by cell-cycle arrest. Tumor cells also release some soluble factors and activate astrocytes and suppress neuronal survival. Astrocytes may also have interactions between microglia and neurons and are also involved in the regulation of tumor cell proliferation by releasing cytokines. Arrows indicate activation or stimulation.

vaded together with cancer cells, gathered to metastatic regions. The brain metastases were often observed in hippocampus and more microglia/macrophages were accumulated in hippocampus than in cerebral cortex, which may indicate an important difference between different region of the brain, though the molecular mechanism is not yet known.

In the present study, microglial cells attenuated the proliferation of HARA-B cells when they were co-cultured. And the inhibitory effect on the proliferation of HARA-B cells was reproduced by microglial conditioned medium. These results suggest that microglial inhibitory effect on the proliferation of HARA-B cells could be conducted through soluble factors released from microglial cells, though such factors are not yet identified. On the other hand, astrocytes enhanced the proliferation of HARA-B cells when they were co-cultured or insert-cultured (data not shown). Unlike microglia-conditioned medium, astrocyte-conditioned medium (ACM) showed little effect on the proliferation of HARA-B cells (data not shown). Therefore it is suggested that microglia express constitutively active factors which inhibit the proliferation of HARA-B cells, while astrocytes need to be activated to release some factors which increase the proliferation of HARA-B cells. A problem on the detection of some soluble factors released from microglia is that cultured murine microglia hardly release measurable cytokines and growth factors unless they are activated, for example by bacterial toxin, lipopolysaccharide. It will be of great interest to identify the factors because they likely possess substantial inhibitory effects on tumor cells with quite low concentration.

Tumor cells also release active factors which activate astrocytes in one hand and inhibit neuronal survival on the other hand, suggesting that they are neurotoxic. It is not known that they are the same factors or not. Tumor-activated astrocytes release several cytokines (data not shown) which increase the proliferation of tumor cells in turn. As for proliferation of tumor cells, the effects of microglia and astrocytes are completely opposite and competing. Likewise, microglia-induced soluble factors and tumor-induced soluble factors might be competing for neuronal survival, since co-existence of microglia attenuated the neurotoxic effects induced by tumor cells. These interactions are shown in Fig. 4.

In conclusion, glial cells (microglia and astrocytes) are associated with tumor development of brain metastasis through the interaction between these two glial cells and tumor cells, as well as interaction between neurons tumor cells in the microenvironment of brain metastasis. Especially microglia plays an important role in inflammatory diseases and traumatic injury in the CNS, a better understanding of microglial function is essential for the development of immune-based treatment strategies against trauma and metastases in the CNS, as well as in brain tumor [18]. The present studies may contribute to understand the mechanism of glial function and may help developing a new strategy for the treatment of brain metastases of peripheral cancer cells.

REFERENCE

[1] *Aloisi F., Care A., Borsellino G., Gallo P., Rosa S., Bassani A., Cabibbo A., Testa U., Levi G., Peschle C.* Production of hemolymphopoietic cytokines (IL-6, IL-8, colony-stimulating factors) by normal human astrocytes in response to IL-1 beta and tumor necrosis factor-alpha. J. Immunol. 149 : 2358—2366. 1992.

[2] *Aloisi F., Ria F., Adorini L.* Regulation of T-cell responses by CNS antigen-presenting cells: different roles for microglia and astrocytes. Immunol. Today. 21 : 141—147. 2000.

[3] *Body J. J., Facon T., Coleman R. E.* A study of the biological receptor activator of nuclear factor-kappaB ligand inhibitor, denosumab, in patients with multiple myeloma or bone metastases from breast cancer. Clin. Cancer Res. 12 : 1221—1228. 2006.

[4] *Davalos D., Grutzendler J., Yang G., Kim J. V., Zuo Y., Jung S., Littman D. R., Dustin M. L., Gan W. B.* ATP mediates rapid microglial response to local brain injury in vivo. Nat. Neurosci. 8 : 752—758. 2005.

[5] *Fidler I. J., Yano S., Zhang R. D. et al.* The seed and soil hypothesis: vascularisation and brain metastases. Lancet Oncol. 3 : 53—57. 2002.

[6] *Galluzzi S., Payne P. M.* Brain metastases from primary bronchial carcinoma: a statistical study of 741 necropsies. Biol. J. Cancer 10 : 408. 1956.

[7] *Hanisch U. K.* Microglia as a source and target of cytokines. Glia. 40 : 140—155. 2002.

[8] *Hertz L., McFarlin D. E., Waksman B. H.* Astrocytes: auxiliary cells for immune responses in the central nervous system? Immunol. Today. 11 : 265—268. 1990.

[9] *Iguchi H., Tanaka S., Ozawa Y., Kashiwakuma T., Kimura T., Hiraga T., Ozawa H., Kono A.* An experimental model of bone metastasis by human lung cancer cells: the role of parathyroid hormone-related protein in bone metastasis. Cancer Res. 56 : 4040—4043. 1996.

[10] *Kim S. U., de Vellis J.* Microglia in health and disease. J. Neurosci. Res. 81 : 302—313. 2005.

[11] *Knights E. M.* Metastatic tumors of the brain and their relation to primary and secondary pulmonary cancer. Cancer 7 : 259. 1954.

[12] *Kreutzberg G. W.* Microglia: a sensor for pathological events in the CNS. Trends. Neurosci. 19 : 312—318. 1996.

[13] *Magilligan D. J., Duvernoy C., Malik G., Lewis J. W., Knighton R., Ausman J. I.* Surgical approach to lung cancer with solitary cerebral metastasis: twenty-five years' experience. Ann. Thorac. Surg. 42 : 360—364. 1986.

[14] *Morony S., Capparelli C., Sarosi I et al.* Osteoprotegerin inhibits osteolysis and decreases skeletal tumor burden in syngeneic and nude mouse models of experimental bone metastasis. Cancer Res. 61 : 4432—4436. 2001.

[15] *Nicolson G. L.* Cancer progression and growth: relationship of paracrine and autocrine growth mechanisms to organ preference of metastasis. Exp. Cell Res. 204 : 171—180. 1993.

[16] *Nimmerjahn A., Kirchhoff F., Helmchen F. R.* Resting microglial cells are highly dynamic surveillants of brain parenchyma in vivo. Science 308 : 1314—1318. 2005.

[17] *Schouten L. J., Rutten J., Huveneers H. A., Twijnstra A.* Incidence of brain metastases in a cohort of patients with carcinoma of the breast, colon, kidney, and lung and melanoma. Cancer. 94 : 2698—2705. 2002.

[18] *Watters J. J., Schartner J. M., Badie B.* Microglia function in brain tumors. J. Neurosci. Res. 81(3) : 447—455. 2005.

[19] *Yoneda T., Hiraga T.* Crosstalk between cancer cells and bone microenvironment in bone metastasis. Biochem. Biophys. Res. Comm. 328 : 679—687. 2005.

[20] *Zhang M., Olsson Y.* Reactions of astrocytes and microglial cells around hematogenous metastases of the human brain. Expression of endothelin-like immunoreactivity in reactive astrocytes and activation of microglial cells. J. Neurol. Sci. 134 : 26—32. 1995.

Поступила 29 V 2009

Clin Exp Metastasis (2009) 26:133–141
DOI 10.1007/s10585-008-9223-x

RESEARCH PAPER

A role for leukemia inhibitory factor in melanoma-induced bone metastasis

Shigeaki Maruta · Soichi Takiguchi · Miho Ueyama · Yasufumi Kataoka · Yoshinao Oda · Masazumi Tsuneyoshi · Haruo Iguchi

Received: 19 May 2008 / Accepted: 10 October 2008 / Published online: 25 October 2008

Abstract Melanoma is commonly associated with multi-organ metastasis, and bone is a frequent metastatic site for melanoma. However, the mechanism responsible for such melanoma-induced bone metastasis is still poorly understood. In the present study, the intracardiac inoculation of leukemia inhibitory factor (LIF)-producing human melanoma-derived cells (SEKI) developed osteolytic bone destruction in male BALB/cA-nu/nu nude mice. To elucidate the role of LIF in melanoma-induced osteolysis, cells were prepared in which the expression of LIF was reduced using a siRNA technique from the parent SEKI cells. Osteoclastogenesis was induced in the co-culture of LIF and/or SEKI cells with osteoblastic stromal cells in vitro, whereas the LIF-reduced SEKI cells did not induce osteoclastogenesis. The intracardiac inoculation of LIF-reduced SEKI cells resulted in a significant reduction in the incidence and number of bone metastasis in comparison to those in the mice inoculated with the parent SEKI cells. The expression of LIF was found in seven of nine human melanoma-derived cell lines, suggesting that LIF expression is a universal event in melanoma. These findings suggest that a potential role for LIF in the melanoma-induced bone metastasis possibly through the stimulation of osteoclastogenesis. LIF might therefore be a potentially effective drug target in the treatment of bone metastasis in melanoma.

Keywords Bone metastasis · Leukemia inhibitory factor · Melanoma · Molecular target · Osteoclastogenesis

Abbreviations

LIF	Leukemia inhibitory factor
PTHrP	Parathyroid hormone-related protein
GAPDH	Glyceraldehydes-3-phosphate dehydrogenase
siRNA	Small interfering RNA
TRAP	Tartrate-resistant acid phosphatase
DAB	3,3′-Diaminobenzidine tetrahydrochloride
HPCs	Hematopoietic cells
OCLs	Osteoclasts
BV	Bone volume
TV	Tissue volume
ES	Eroded bone surface
BS	Bone surface

Introduction

Metastasis is a common phenomenon in the course of malignant tumors, and bone is a frequently affected as a metastatic site in certain types of cancers, including breast cancer, prostate cancer, lung cancer and melanoma. Bone metastasis is associated with substantial morbidity, including bone pain, pathological fractures, neurological

S. Maruta · S. Takiguchi
Institute for Clinical Research, National Kyushu Cancer Center, Fukuoka 811-1395, Japan

M. Ueyama · Y. Kataoka
Department of Pharmaceutical Care and Health Sciences, Faculty of Pharmaceutical Sciences, Fukuoka University, Fukuoka 814-0180, Japan

Y. Oda · M. Tsuneyoshi
Department of Anatomical Pathology, Graduate school of Medical Sciences, Kyushu University, Fukuoka 812-8582, Japan

H. Iguchi (✉)
Clinical Research Institute, Shikoku Cancer Center, Minamiumemotomachi Ko160, Matsuyama, Ehime 791-0280, Japan
e-mail: higuchi@shikoku-cc.go.jp

deficit and/or hypercalcemia, thus the management of bone metastasis is a clinically significant issue in patients with malignant tumors.

In bone metastasis, the primary mechanism responsible for bone destruction is tumor cell-mediated stimulation of osteoclastic bone resorption [1]. Several factors, including parathyroid hormone-related protein (PTHrP) [2], RANKL [3], and MIP-1α [4], are implicated in this mechanism. These factors, released by tumor cells, stimulate the osteoclast activation either directly or through osteoblasts, thus leading to osteolysis and the release of tumor cell growth factors from the bone matrix. Among them, PTHrP seems to be a major regulator by stimulating osteoclastic bone resorption through upregulation of RANKL in osteoblasts in lung and breast cancer [2, 5]. A humanized monoclonal antibody against PTHrP has been generated [6], and its effect on bone metastasis in cancer patients is under investigation. However, the mechanism responsible for bone destruction in melanoma is still poorly understood. A human melanoma-derived cell line (SEKI) was established from a tumor in the lower leg skin of a 28-year-old female [7]. SEKI-bearing nude mice revealed cachexia [8], and subsequently, leukemia inhibitory factor (LIF) was identified as a cachexic factor from SEKI cells [9]. LIF was first isolated as a factor which induced macrophage differentiation from M1 murine myeloid leukemic cells and suppressed their proliferation in vitro [10]. Subsequent studies demonstrated multiple functions of LIF [11, 12], including stimulation of osteoclastogenesis [13]. It is important to identify any factors that are involved in bone destruction since such factors could be an attractive therapeutic target. This study describes experimental evidence of the role of LIF in the progression of bone metastasis in melanoma.

Materials and methods

Cell culture

LIF-producing SEKI cells were purchased from the Health Science Research Resources Bank (Osaka, Japan), and used in the present study. Eight human melanoma-derived cell lines (A375, Hs700T, SK-MEL-19, SK-MEL-28, SK-MEL-164, MeWo, G361, and COLO38) were also used to assay the expression of LIF and PTHrP. These cell lines were purchased from American Type Culture Collection (Rockville, MD, A375, Hs700T, SK-MEL-28, and MeWo) and Health Science Research Resources Bank (Osaka, Japan, G361) and/or were kindly provided by Dr Toshirou Kageshita (Department of Dermatology, Faculty of Medicine, Kumamoto University, Kumamoto, Japan, COLO38, SK-MEL-19, and SK-MEL-164).

SEKI, COLO38, G361, SK-MEL-19, SK-MEL-28 and SK-MEL-164 were cultured in RPMI 1640 medium (Gibco, Grand Island, NY) supplemented with 10% FBS and 50 units/ml of penicillin and streptomycin in a humidified atmosphere under 5% CO_2 at 37°C. A375 and Hs700T were cultured in Dulbecco's modified Eagle medium (Gibco) supplemented with 10% FBS and 50 units/ml of penicillin and streptomycin under the same conditions described above. MeWo was cultured in minimum essential medium (Gibco) supplemented with 10% FBS and 50 units/ml of penicillin and streptomycin under the same conditions described above.

Total RNA preparation, reverse transcription, and semi-quantitative PCR

Total RNA was extracted from various cultured human melanoma cells using the Qiagen RNeasy kit (Qiagen, Valencia, CA) according to the manufacturer's protocol. RT-PCR was performed using the ThermoScript RT-PCR System (Invitrogen, Carlsbad, CA) according to the manufacturer's protocol. The PCR primer pairs were 5′-CAG CCCATAATGA AGGTCTTGGCGG-3′ and 5′-GGCAC TGGGGTT GAGGATCT-3′ for the detection of leukemia inhibitory factor (LIF) mRNA, and 5′-ACAGTCCATGC CATCACTGCC-3′ and 5′-GCCTGCTTCACCACCTTCT TG-3′ for the detection of glyceraldehydes-3-phosphate dehydrogenase (GAPDH). PCR conditions were 94°C (1 min), 30 cycles of 94°C (30 s), 62°C (30 s) and 72°C (1 min 30 s), and 72°C (3 min) for the detection of LIF mRNA, and 94°C (1 min), 25 cycles of 94°C (1 min), 58°C (2 min) and 72°C (2 min), and 72°C (3 min) for the detection of GAPDH mRNA. A 20 μl portion of the reaction mixture contained 80 ng of cDNA, 1× ExTaq buffer, 2.5 mM $MgCl_2$, 0.2 mM dNTP mixture, 0.5 μM paired primers and 1 unit ExTaq (Takara, Tokyo, Japan). PCR products were separated on 2% agarose gel (Sigma, St. Louis, MO) in 1× TAE buffer.

RNA interference assay

The expression of LIF was silenced using the pSilencer 2.0-U6 (Ambion Inc., Austin, TX). The 60-mers complementary oligonucleotides encoding a 19-mer hairpin sequence specific to the human LIF (GenBank/EMBL/DDBJ databanks accession number NM002309) mRNA (nucleotides 367–385; 5′-GCTGGTGGAGCTGTACCGC-3′, nucleotides 589–607; 5′-GGATGTCTTCCAG AAGA AG-3′ or nucleotides 640–658; 5′-GCAGATCATCGCCG TGTTG-3′), a loop sequence (TTCAAGAGA) separating the two complementary domains, and a polythymidine tract (TTTTTT) to terminate transcription were synthesized and ligated into the pSilencer 2.0-U6 vector. The derived